Mechanistic principles underlying regulation of the actin cytoskeleton by phosphoinositides

Yosuke Senju[a], Maria Kalimeri[b], Essi V. Koskela[a,1], Pentti Somerharju[c], Hongxia Zhao[a], Ilpo Vattulainen[b,d], and Pekka Lappalainen[a,2]

[a]Institute of Biotechnology, University of Helsinki, FI-00014 Helsinki, Finland; [b]Department of Physics, Tampere University of Technology, FI-33101 Tampere, Finland; [c]Faculty of Medicine, University of Helsinki, FI-00014 Helsinki, Finland; and [d]Department of Physics, University of Helsinki, FI-00014 Helsinki, Finland

Edited by Kai Simons, Max Planck Institute of Molecular Cell Biology and Genetics, Dresden, Germany, and approved September 14, 2017 (received for review March 29, 2017)

The actin cytoskeleton powers membrane deformation during many cellular processes, such as migration, morphogenesis, and endocytosis. Membrane phosphoinositides, especially phosphatidylinositol 4,5-bisphosphate [PI(4,5)P_2], regulate the activities of many actin-binding proteins (ABPs), including profilin, cofilin, Dia2, N-WASP, ezrin, and moesin, but the underlying molecular mechanisms have remained elusive. Moreover, because of a lack of available methodology, the dynamics of membrane interactions have not been experimentally determined for any ABP. Here, we applied a combination of biochemical assays, photobleaching/activation approaches, and atomistic molecular dynamics simulations to uncover the molecular principles by which ABPs interact with phosphoinositide-rich membranes. We show that, despite using different domains for lipid binding, these proteins associate with membranes through similar multivalent electrostatic interactions, without specific binding pockets or penetration into the lipid bilayer. Strikingly, our experiments reveal that these proteins display enormous differences in the dynamics of membrane interactions and in the ranges of phosphoinositide densities that they sense. Profilin and cofilin display transient, low-affinity interactions with phosphoinositide-rich membranes, whereas F-actin assembly factors Dia2 and N-WASP reside on phosphoinositide-rich membranes for longer periods to perform their functions. Ezrin and moesin, which link the actin cytoskeleton to the plasma membrane, bind membranes with very high affinity and slow dissociation dynamics. Unlike profilin, cofilin, Dia2, and N-WASP, they do not require high "stimulus-responsive" phosphoinositide density for membrane binding. Moreover, ezrin can limit the lateral diffusion of PI(4,5)P_2 along the lipid bilayer. Together, these findings demonstrate that membrane-interaction mechanisms of ABPs evolved to precisely fulfill their specific functions in cytoskeletal dynamics.

actin cytoskeleton | phosphoinositides | protein–lipid interactions | signal transduction | molecular dynamics simulations

Polymerization of actin filament networks against membranes provides forces for many vital cellular processes, including generation of plasma membrane protrusions in cell migration and morphogenesis, as well as the formation of plasma membrane invaginations in endocytosis (1, 2). The dynamics and the 3D organization of actin filament arrays in these processes are precisely controlled by a large array of actin-binding proteins (ABPs), whose activities are in turn regulated by various signaling pathways (3–5). In addition to kinase/phosphatase cascades, which can activate or inhibit central actin-regulatory proteins, membrane phospholipids, especially phosphatidylinositol 4,5-bisphosphate [PI(4,5)P_2] and phosphatidylinositol 3,4,5-trisphosphate [PI(3,4,5)P_3], have emerged as important regulators of actin dynamics. PI(3,4,5)P_3 contributes to actin dynamics mainly by regulating the Rho family small GTPases, whereas PI(4,5)P_2 controls cytoskeletal dynamics more directly by regulating ABPs (6).

PI(4,5)P_2, which is the most abundant phosphorylated derivative of phosphatidylinositol at the plasma membrane, interacts with multiple ABPs. PI(4,5)P_2 typically inhibits proteins that catalyze actin filament disassembly [e.g., actin-depolymerizing factor (ADF)/cofilins, gelsolin, and twinfilin] or prevent the assembly of new actin monomers into filament ends (e.g., heterodimeric capping protein) (7–10). Conversely, PI(4,5)P_2 activates proteins that promote actin filament assembly (e.g., N-WASP) or function as linkers between actin filaments and the plasma membrane (e.g., ezrin, moesin, radixin, and talin) (11–15). As a result, an increase in the plasma membrane PI(4,5)P_2 induces actin filament assembly beneath the membrane, whereas decreasing the levels or availability of PI(4,5)P_2 at the plasma membrane diminishes actin filament assembly and enhances filament disassembly (16–19). Cell biological studies have also provided evidence that membrane interactions are critical for the proper in vivo functions of many ABPs, including cofilin, vinculin, formins, and N-WASP (20–25).

Despite the central biological roles of ABPs, the molecular mechanisms by which they interact with cellular membranes remain largely unknown. So far, atomistic details, as derived by a combination of mutagenesis and molecular dynamics simulation approaches, have been reported only for membrane interactions of the heterodimeric capping protein (26, 27), whereas, for other central ABPs, the principles of membrane interactions have remained elusive. Moreover, whether distinct ABPs interact with membranes through similar or different affinities has not been reported. Most importantly, the dynamics of membrane interactions have not been experimentally determined for any ABP. The kinetics of membrane interactions have fundamental consequences for the cellular functions of proteins. This is because the membrane

Significance

Membrane phosphoinositides have emerged as key regulators of the actin cytoskeleton in cell migration, morphogenesis, cytokinesis, and endocytosis. However, the molecular mechanisms by which actin-binding proteins (ABPs) interact with phosphoinositide-rich membranes remain remarkably poorly understood. By applying a combination of biochemical, biophysical, and atomistic molecular dynamics simulation approaches on six central ABPs, we discovered that they employ multivalent electrostatic interactions for membrane binding. Strikingly, our experiments revealed that these proteins display enormous differences in their membrane interaction dynamics and in the ranges of phosphoinositide densities that they sense. These differences precisely correlate with the specific functions of these proteins in cytoskeletal dynamics. These findings uncover molecular principles by which membrane phosphoinositides regulate dynamics and architecture of the actin cytoskeleton in cells.

Author contributions: Y.S., M.K., H.Z., I.V., and P.L. designed research; Y.S., M.K., E.V.K., and P.S. performed research; Y.S. and M.K. analyzed data; and Y.S., M.K., I.V., and P.L. wrote the paper.

The authors declare no conflict of interest.

This article is a PNAS Direct Submission.

[1]Present address: Department of Bioproducts and Biosystems, Aalto University, 00076 Aalto, Finland.

[2]To whom correspondence should be addressed. Email: pekka.lappalainen@helsinki.fi.

This article contains supporting information online at www.pnas.org/lookup/suppl/doi:10.1073/pnas.1705032114/-/DCSupplemental.

association and dissociation rates, as well as the lateral mobility of proteins along the membrane plane, determine their subcellular localization, their accessibility to other interaction partners, and the effects of "stimulus-responsive" PI(4,5)P_2 synthesis/hydrolysis on their functions. For example, cell biological studies suggested that cofilin stably binds to the plasma membrane in carcinoma cells and is released only following epidermal growth factor-induced PI(4,5)P_2 hydrolysis (21, 28, 29). Moreover, some animal, plant, and slime mold formins, which promote actin filament nucleation and elongation, were proposed to require the N-terminal phosphoinositide-binding region for proper anchoring to the plasma membrane (20, 30–33). However, such functions would require stable, high-affinity binding of these proteins to the PI(4,5)P_2-rich membranes, which has not been experimentally demonstrated.

Here, we applied a combination of biochemical, biophysical, and atomistic molecular dynamics simulation approaches to reveal how central ABPs cofilin, profilin, Dia2 formin, N-WASP, ezrin, and moesin interact with PI(4,5)P_2-rich membranes. Furthermore, we developed photobleaching and photoactivation-based assays on reconstituted membrane systems to determine the kinetics of ABP–membrane interactions. These studies uncovered that, although these proteins interact with membranes mainly through electrostatic interactions, they display drastic differences in the affinities and dynamics of membrane interactions. Interestingly, these distinct membrane-interaction kinetics correlate with the roles of these proteins in cytoskeletal dynamics.

Results

ABPs Display Drastic Differences in Binding to Phosphoinositide-Rich Membranes. To elucidate the molecular mechanisms by which PI(4,5)P_2 regulates actin dynamics, we focused on the membrane interactions of six conserved ABPs: profilin-1, cofilin-1, Dia2, N-WASP, ezrin, and moesin. We chose these proteins for the study because (*i*) they represent functionally different classes of actin regulatory proteins, (*ii*) the effects of phosphoinositides on their activities are well established, and (*iii*) their membrane-binding regions have been mapped by mutagenesis analyses. Nontagged and sfGFP/mCherry fusions of these proteins were expressed and purified for biochemical and in vitro imaging experiments, respectively (Fig. S1 *A* and *B*). ADF/cofilins and profilins are small globular proteins, which interact with phosphoinositides and actin through partially overlapping surfaces (34–37). Thus, full-length proteins of the major mammalian isoforms, profilin-1 and cofilin-1, were purified for our assays. Given that Dia2, N-WASP, ezrin, and moesin are large multidomain proteins that exist as autoinhibited structures, their membrane-binding domains (polybasic regions of Dia2 and N-WASP and the FERM domains of ezrin and moesin) (13, 20, 38, 39) were produced for these experiments (Fig. 1*A*).

We first performed cosedimentation and coflotation assays with vesicles containing 10 mol% PI(4,5)P_2 to determine the membrane-binding affinities of these proteins under physiological salt conditions. Strikingly, we found drastic differences in their interactions with membranes (Fig. 1*B* and Fig. S2). The FERM domains of ezrin and moesin bound phosphoinositide-rich vesicles with very high affinity (apparent $K_d \sim 5$ μM). The lipid-binding domains of Dia2 and N-WASP displayed intermediate membrane-binding affinities (apparent $K_d \sim 100$ μM), whereas profilin-1 and cofilin-1 bound membranes with only very modest affinity that was more than two orders of magnitude less than those of ezrin and moesin (Fig. 1*C*). We confirmed these results by visualizing the association of mCherry-tagged ABPs with giant unilamellar vesicles (GUVs) by confocal microscopy (Fig. 1*D*). The mCherry-tagged proteins were added on GUVs containing TopFluor-labeled PI(4,5)P_2, and the fluorescence intensities of mCherry-tagged proteins on GUVs were quantified (Fig. 1*E*). Consistent with the cosedimentation and coflotation results, the FERM domains of ezrin and moesin bound strongly to the GUVs, the basic domains of Dia2 and N-WASP showed intermediate binding, whereas profilin-1 and cofilin-1 displayed only very weak associations with GUVs.

N-WASP and cofilin-1 were previously shown to function as phosphoinositide density sensors (36, 38). Therefore, we examined whether a local increase in the PI(4,5)P_2 density on the membrane affects the membrane binding of other ABPs as well. Cosedimentation assays revealed that all six proteins exhibited an increase in membrane binding with respect to PI(4,5)P_2 concentration, suggesting that they can sense the local density of PI(4,5)P_2 on the membrane (Fig. S3). The binding curves displayed sigmoidal functions, at least for profilin-1, cofilin-1, Dia2, and N-WASP, and Hill coefficients (nH) were greater than 1 [profilin-1 nH = 3.7; cofilin-1 nH = 4.2; Dia2 basic domain (BD) nH = 3.0; N-WASP polybasic motif and GTPase binding domain (B-GBD) nH = 2.3], indicating cooperative membrane binding with respect to the PI(4,5)P_2 density in the membranes. Importantly, whereas binding of the FERM domains of ezrin and moesin saturated at ∼2 mol%, PI(4,5)P_2, ∼10 mol% PI(4,5)P_2 was required for full binding of Dia2 and N-WASP domains, and ∼20 mol% PI(4,5)P_2 was required to saturate cofilin-1 and profilin-1 binding to the membrane. Furthermore, only ∼50% of cofilin-1 and profilin-1 cosedimented with vesicles even at a very high PI(4,5)P_2 density (40 mol%; Fig. S3). Thus, cofilin-1 and profilin-1 bind membranes with low affinity even at conditions in which the PI(4,5)P_2 density is not limiting.

Collectively, these experiments revealed that central ABPs display enormous differences in their affinities to phosphoinositide-rich membranes, and that they sense PI(4,5)P_2 densities at very different ranges. Cofilin-1 and profilin-1 display only low-affinity interactions with membranes and require very high phosphoinositide density, whereas Dia2, N-WASP, and especially ezrin and moesin bind membranes with much higher affinities and their binding saturates at lower phosphoinositide densities.

ABPs Interact with Membranes Through Electrostatic Interactions. We next examined whether the drastic differences in membrane affinities of ABPs arise from distinct membrane-interaction mechanisms. Whether ABPs associate with phospholipid-rich membranes through electrostatic interactions, via specific binding pockets for lipid head groups, and/or interact with the acyl-chain region of the lipid bilayer has not been examined in most cases. Even when this has been experimentally approached, the results have remained contradictory (36, 40). To test the contribution of electrostatic interactions, we performed liposome cosedimentation assays with different NaCl concentrations: 0 mM, 100 mM, and 400 mM. In all cases, the amounts of cosedimenting proteins decreased with increasing NaCl concentration, suggesting that membrane interactions of all six ABPs are electrostatic in nature (Fig. 2 *A* and *B*). Furthermore, cosedimentation assays carried out with cofilin-1, N-WASP, and moesin did not reveal clear specificity toward any phosphoinositide (Fig. S4). Instead, their binding appeared to correlate with the net negative charge of the phospholipids, i.e., these proteins preferentially bound to PIP_2 and PIP_3 compared with phosphatidylserine (PS), phosphatidylinositol, or monophosphorylated phosphoinositide.

To examine possible contributions of hydrophobic interactions, we applied a diphenylhexatriene (DPH) anisotropy assay. An increase in DPH anisotropy indicates insertion of proteins into the lipid bilayer (41). Compared with the I-BAR domain of MIM, which inserts an amphipathic helix into the bilayer (42) and was used as a positive control, the values of DPH anisotropy did not significantly increase upon addition of the ABPs examined here, indicating that they do not exhibit deep insertions into the lipid bilayer (Fig. 2*C*).

Together, these experiments provide evidence that cofilin-1, profilin-1, Dia2, N-WASP, ezrin, and moesin neither harbor binding pockets for specific phosphoinositide head groups nor associate with the acyl-chain region of the lipid bilayer. Instead, they interact with the phosphoinositide head groups through multivalent electrostatic interactions, enabling them to function as sensors of membrane phosphoinositide density.

Molecular Mechanisms of Membrane Interactions of Cofilin and Moesin. To gain insights into the mechanisms underlying different affinities of ABPs to the membrane, and to reveal the molecular

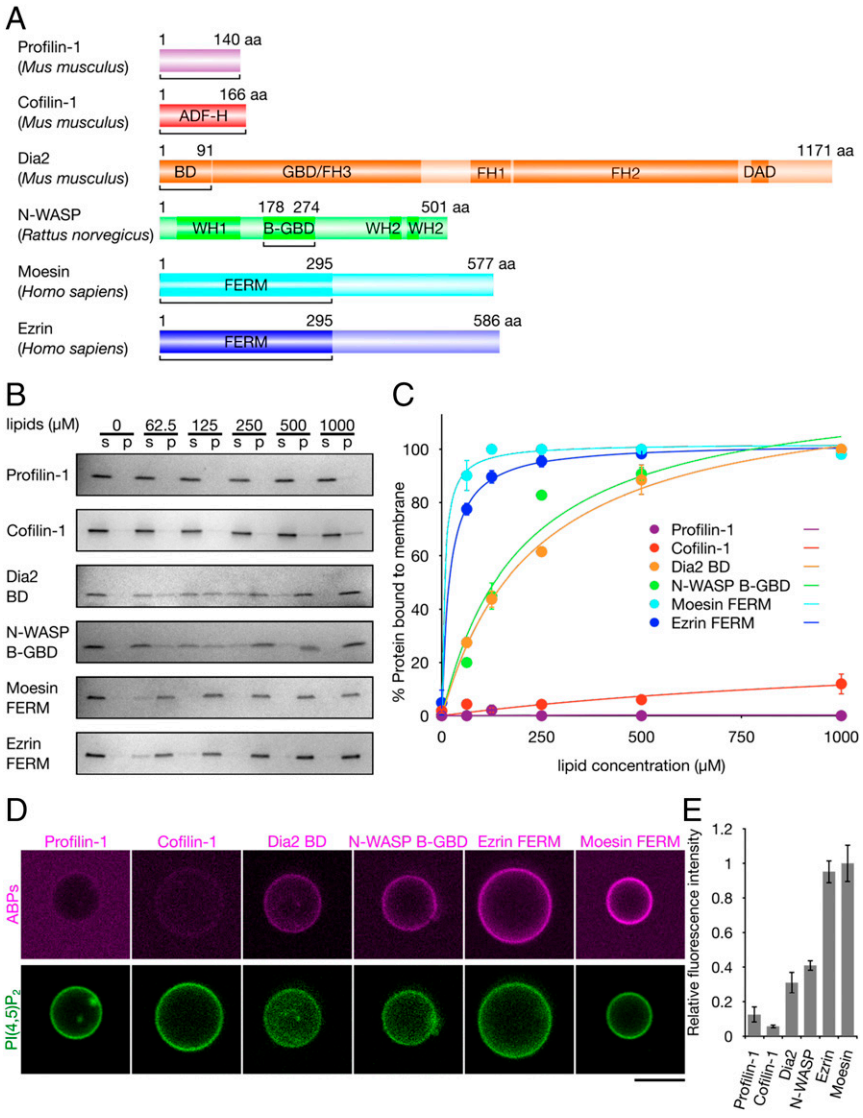

Fig. 1. Diverse affinities of ABPs for $PI(4,5)P_2$-containing membranes. (*A*) Domain structures of ABPs used in this study. The protein regions used in the experiments are underlined. ADF-H, ADF homology; BD, basic domain; DAD, diaphanous autoregulatory domain; GBD, GTPase-binding domain; FH, formin homology; WH, WASP homology. (*B*) Liposome cosedimentation assay with increasing lipid concentrations from 0 to 1,000 μM. "S" indicates the supernatant and "P" indicates the pellet containing the protein-bound liposomes. The lipid composition was POPC:POPE:POPS:$PI(4,5)P_2$:rhodamine DHPE (50:19.5:20:10:0.5, mol/mol). The concentration of each ABPs was 1 μM. (*C*) Membrane-binding ratios of ABPs with increasing lipid concentrations (n = 3; mean ± SE). The data were fitted with the least-squares methods. (*D*) The binding of 10 μM mCherry-tagged ABPs on GUVs containing TopFluor-labeled $PI(4,5)P_2$. The lipid composition was POPC:POPE:POPS:$PI(4,5)P_2$ (58:20:20:2, mol/mol). (Scale bar, 10 μm.) (*E*) Fluorescence intensities of the mCherry-tagged ABPs on the GUVs. The values were normalized with respect to the fluorescence intensity of the FERM domain of moesin, and these values indicate the amount of ABPs bound to the GUVs (n = 10; mean ± SE).

principles of ABP–lipid interactions, we performed atomistic molecular dynamics simulations for two extreme cases: cofilin-1 and the FERM domain of moesin, whose structures are available (43, 44). In both cases, residues important for lipid binding have been mapped by mutagenesis (13, 36, 39).

We first performed unbiased 200-ns simulations, in three independent replicates for each protein, to explore the binding of the proteins on a lipid bilayer whose composition matched the one used in experiments (Movies S1 and S2). At the beginning, both proteins were placed slightly above the bilayer (~0.5 nm) with the known binding surfaces facing the membrane. As confirmed by saturation of the average number of hydrogen bonds between the protein and the lipids, equilibrium behavior was reached within 50–60 ns for cofilin-1, and within 150 ns for the FERM domain of moesin, averaged over the three replicates (Fig. S5). The slower equilibration of the moesin FERM domain compared with cofilin-1 most likely arises from its larger size (radius of gyration) given that increasing protein size slows down diffusion and rotational motion. Fig. 3, *Left*, shows the time evolution of the number of residues in contact with the bilayer, averaged over the three replicates. Importantly, also the number of positively charged, lipid-bound residues of cofilin-1 (Fig. 3*A*) was smaller than that for the FERM domain of moesin (Fig. 3*B*).

Overall, both proteins used a large, relatively flat, positively charged surface to interact simultaneously with several negatively charged lipid head groups (Fig. 3). After equilibration, cofilin-1 interacted with an average of 3.0 ± 0.1 $PI(4,5)P_2$ head groups, whereas the moesin FERM domain bound to an average of 6.0 ± 0.3 $PI(4,5)P_2$ head groups (Fig. 4). In both cases, there was a comparable average number of bound PS lipids, suggesting a nonspecific electrostatic interaction between protein and lipids. It is worth noting that the density of PS was two times higher, yet the interaction with $PI(4,5)P_2$ was pronounced as a result of the stronger negative charge of $PI(4,5)P_2$ and the larger size of the $PI(4,5)P_2$ head group, which allows more effective binding with positive ion pairs in the protein. Please note that, despite the asymmetry in the composition of the bilayer, we did not detect significant effects on membrane curvature for the time scales explored in our simulations.

All simulations reproduced the charged phosphoinositide-binding residues identified in the previous mutagenesis experiments (13, 36, 39). They revealed additional positively charged lipid-binding residues in the moesin FERM domain (Lys3, Lys35, Arg40, Lys72, Arg246, Lys254, Lys258, Lys262, Lys263) in addition to the previously identified residues (Lys53, Lys60, Lys64, Lys63, Lys83, Lys253, Lys278, Arg273, Arg275, Arg279, Arg293). The results of two additional 500-ns simulations, one for each protein, in which the protein started from a larger distance from the bilayer, were in agreement with the shorter simulations (Fig. S6 and Movies S3 and S4). Furthermore, the simulation for cofilin-1 suggested that the

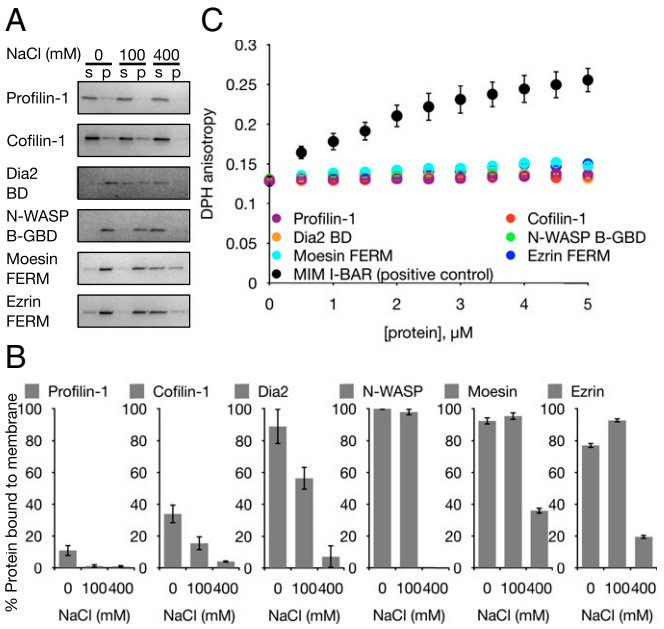

Fig. 2. ABPs bind to PI(4,5)P_2-rich membranes through electrostatic interactions. (*A*) Salt sensitivity of interactions of ABPs with liposomes. The NaCl concentration was varied from 0 mM to 400 mM, and liposome cosedimentation assays were performed. "S" indicates the supernatant and "P" indicates the pellet containing the protein-bound liposomes. The lipid composition was POPC:POPE:POPS:PI(4,5)P_2:rhodamine DHPE (50:19.5:20:10:0.5, mol/mol). (*B*) Quantification of the ratio of ABPs bound to the liposomes ($n = 3$; mean ± SE). Salt concentration inversely correlated with the amount of cosedimenting protein, indicating electrostatic interactions between the proteins and the membrane. (*C*) DPH anisotropy assay for detecting possible insertion of proteins into the acyl-chain region of the bilayer. DPH anisotropy increased in the presence of MIM-I-BAR (positive control), indicating penetration of this protein into the lipid bilayer. Note that the ABPs studied here did not significantly increase the DPH anisotropy ($n = 3$; mean ± SE).

binding to the membrane is driven by helix-4 (Leu111-Thr129) given that the anchoring onto the bilayer was initiated by residues Lys112, Lys126, and Lys127 (Movie S3). For both proteins, the residues interacting with the membrane extended over a large surface to mediate dynamic, "unspecific" electrostatic interactions, whereas no specific binding pockets with lipid head groups were observed. The simulations indicated that the moesin residues K83 and R293, which were previously found to lie inside a putative binding pocket (39), showed weak or no interactions with lipids (Movie S1). Moreover, no substantial insertion of the protein into the hydrophobic core of the bilayer was detected in any of the simulations.

To estimate the free energy of membrane binding of cofilin-1 and the FERM domain of moesin, we performed umbrella sampling simulations by using the final protein-membrane conformations obtained from the unbiased simulations. The free energy of binding was quantified as 12 ±2 kcal/mol for cofilin-1 and 33 ±2 kcal/mol for the FERM domain of moesin (Fig. 5), highlighting that cofilin-1 is considerably more weakly bound to the membrane.

Together, these simulation experiments revealed the molecular principles by which cofilin-1 and the FERM domain of moesin associate with phosphoinositide-rich membranes. The atomistic simulation data are consistent with the results from the biochemical experiments described here earlier, and provide an atomistic-scale explanation for the higher membrane-binding affinity of the FERM domain of moesin compared with cofilin-1.

Dynamics of ABP–Membrane Interactions. We next developed in vitro imaging approaches to determine the membrane-binding kinetics of these proteins. For fluorescence recovery after photobleaching (FRAP) experiments, superfolder GFP (sfGFP)-tagged proteins were expressed and purified (Fig. S1*B*). Because many ABPs harbor cysteines on the surfaces involved in lipid interactions, we chose to use fluorescent fusion proteins rather than cysteine-conjugated fluorophores in our study; these fluorescent tags did not disturb the membrane binding of ABPs (Fig. S1*C*). As cofilin-1 and profilin-1 bind membranes only with a very low affinity (Fig. 1 *B* and *C*) and associate weakly with GUVs at physiological salt conditions (Fig. 1 *D* and *E*), they were excluded from the analysis. Thus, we focused on determining the dynamics of Dia2, N-WASP, and ezrin FERM domain on membranes. In the first set of experiments, sfGFP-tagged proteins were administered to the outside of GUVs, and entire GUVs were photobleached. With this approach, we can exclude the contributions from lateral diffusion, and the fluorescence recovery should thus reflect the combination of protein association/dissociation to/from the membrane (Fig. 6*A*). Importantly, these experiments revealed that the fluorescence recovery of the FERM domain of ezrin was extremely slow, whereas the lipid-binding domains of Dia2 and N-WASP displayed somewhat more rapid recovery on GUVs (Fig. 6 *B* and *C*).

Because FRAP experiments cannot distinguish between membrane association and dissociation, we next employed a photoactivation approach to elucidate whether the slow dynamics of these proteins is because of their slow association with or slow dissociation from the membranes (Fig. 6*D*). We purified

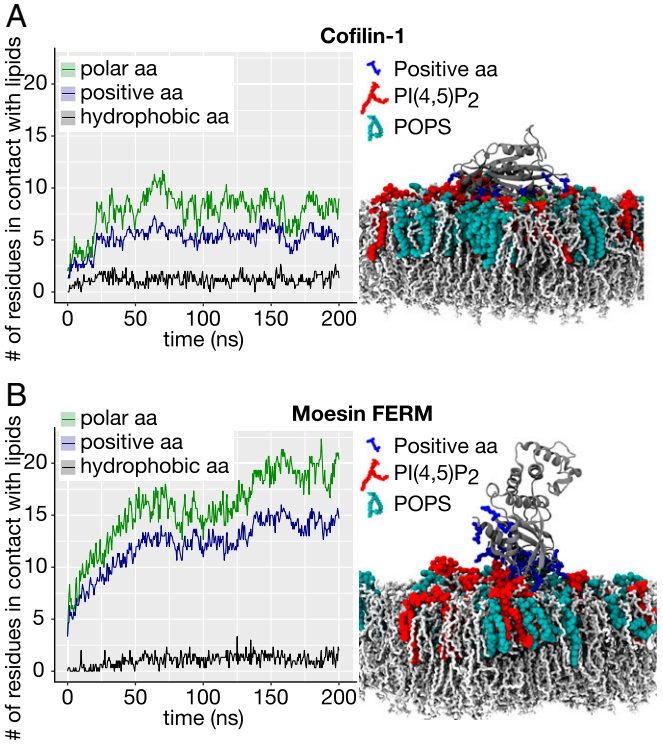

Fig. 3. Molecular mechanisms of cofilin-1 and moesin FERM domain interactions with membranes as determined by atomistic molecular dynamics simulations: (*A*) Cofilin-1 and (*B*) moesin FERM domain. (*Left*) Average numbers, over three independent simulations, of protein residues in contact with lipids. Polar, positively charged, and hydrophobic residues are shown with green, blue, and black lines, respectively. Excluding the first 50 ns in each case, the total average numbers of polar protein–lipid contacts were 8.4 ± 0.9 and 17.2 ± 2.0 for cofilin-1 and the FERM domain of moesin, respectively. (*Right*) Conformation of each protein-bilayer system after 200 ns of unbiased simulation. Positively charged residues that were found to interact with lipids are shown in a blue "licorice" representation. PI(4,5)P_2 and PS molecules are shown in red and cyan, respectively.

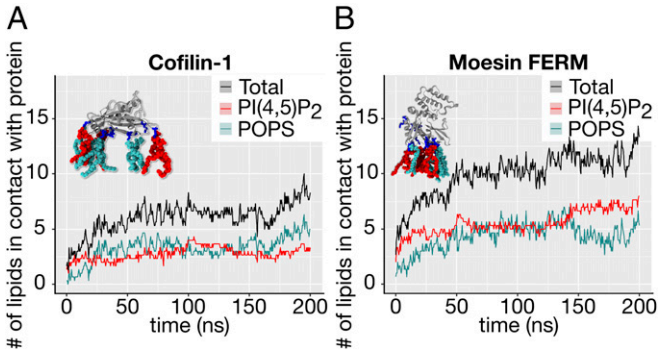

Fig. 4. Average number of protein-bound, negatively charged lipids in the 200-ns unbiased simulations: (*A*) Cofilin-1 and (*B*) the moesin FERM domain. $PI(4,5)P_2$ and POPS molecules are shown in red and cyan, respectively. (*Inset*) Representative final conformations of each protein with the respective bound negative lipids. Positively charged residues of the protein that were found to form contacts with lipids in at least one of the simulations are shown in a blue licorice representation.

the lipid-binding domains of Dia2, N-WASP, and ezrin as photoactivatable GFP (paGFP)-fusion proteins, administered them to the outside of GUVs, and activated entire GUVs with a 405-nm UV laser. The fluorescence decay of paGFP on the GUVs was followed, as this reflects the dissociation rate (k_{off}) of the proteins from the membranes. These experiments revealed that the FERM domain of ezrin displayed extremely slow dissociation from the membrane (fluorescence decay during the 60-s observation period was ~10%), whereas the dissociation of lipid-binding domains of Dia2 and N-WASP was more rapid characterized by ~20–30% fluorescence decay during the 60-s observation period (Fig. 6 *E* and *F*). The photoactivation results were consistent with the FRAP data, and the small differences between the rates of fluorescence recoveries and decays in these assays may result from photobleaching during the detection periods. Thus, the slow dynamics of these proteins arise mainly from their slow k_{off} rates from the phosphoinositide-rich membranes.

Lateral Diffusion of ABPs and $PI(4,5)P_2$. In addition to protein association/dissociation at the membrane, lateral diffusion along the membrane may be critical for the functions of membrane-associated proteins. To examine lateral diffusion of ABPs as well as the protein-associated $PI(4,5)P_2$ along the bilayer, we photobleached a segment of the GUVs, and subsequently measured the fluorescence recovery of the mCherry-fusion proteins and TopFluor $PI(4,5)P_2$ (Fig. 7*A*). Please note that, as a result of the slow dissociation of these proteins from the membrane (Fig. 6), the recovery of the bleached segments is dominated by lateral diffusion of the protein. Moreover, the fluorescence intensities do not recover to the initial level after photobleaching because ~20% of the fluorescent molecules are bleached on the GUVs. These experiments revealed that lateral diffusion of the FERM domain of ezrin on GUVs was slow compared with that of the lipid-binding domains of Dia2 and N-WASP. Similar results were obtained with GUVs containing 2 mol% $PI(4,5)P_2$ and 10 mol% $PI(4,5)P_2$. This slow diffusion may be a result of protein crowding or assembly of the ezrin FERM domain into large oligomers. Furthermore, lateral diffusion of $PI(4,5)P_2$ diminished in the presence of 10 μM ezrin FERM domain (diffusion coefficient $D = 0.68$ μm^2/s) compared with that in the absence of proteins ($D = 2.5$ μm^2/s) or in the presence of 10 μM Dia2 or N-WASP (Fig. 7 *B* and *D*).

The dynamics of cofilin-1, the lipid-binding domains of N-WASP, and the FERM domain of ezrin were also examined in cells (Fig. S7). Here, sfGFP-tagged proteins were expressed in B16-F1 cells (Fig. S7*A*), and FRAP was applied to determine their dynamics at a region close to the cell edge (Fig. S7*B*). Ezrin FERM domain typically displayed a relatively uniform localization along the cell cortex compared with lamellipodial accumulation of cofilin-1 and Dia2 (20) (Fig. S7 *A* and *B*). Moreover, fusing the FERM domain to the actin polymerization-promoting FH1-FH2 fragment of Dia2 resulted in more uniform actin filament assembly at the cell periphery compared with the filopodia-concentrated actin filament assembly by the isolated FH1-FH2 domain (Fig. S7*D*). Consistent with our in vitro experiments, FRAP analysis revealed that the kinetics of the FERM domain of ezrin were slow at the vicinity of the plasma membrane. The lipid-binding domain of N-WASP displayed intermediate dynamics, and cofilin-1 fluorescence recovered rapidly at the membrane (Fig. S7 *B* and *C*). Please note that, in FRAP experiments carried out on cells, it is technically not possible to distinguish between rapid lateral diffusion and rapid dissociation of a protein from the membrane. Hence, the more rapid dynamics of N-WASP and the FERM domain of ezrin in cells compared with the GUVs are likely to arise from their rapid lateral diffusion. In this context, it is important to note that, at lower concentration (1 μM), the ezrin FERM domain also displayed relatively rapid lateral diffusion on GUVs, most likely because of a lack of protein crowding or efficient protein oligomerization at the membrane (Fig. S8 *A–D*).

Together, our in vitro FRAP and photoactivation experiments revealed that the FERM domain of ezrin exhibits very slow dissociation from the membrane. In addition, it displays slow lateral diffusion along the membrane and can limit the mobility of $PI(4,5)P_2$. The lipid-binding domains of Dia2 and N-WASP display relatively slow dissociation from the membrane, but they undergo rapid lateral diffusion along the membrane plane.

Discussion

The dynamics and 3D architecture of the actin cytoskeleton are controlled by plasma membrane phospholipids, but the underlying mechanisms have remained poorly understood. Here we revealed that, although different actin-regulatory proteins interact with membranes through distinct domains, they bind phosphoinositide-rich membranes by using similar multivalent electrostatic interactions and can thus function as sensors of phosphoinositide density at the membrane. Importantly, our experiments revealed that ABPs display enormous differences in their affinities for membranes and in the ranges of phosphoinositide densities that they sense. By developing photobleaching and photoactivation approaches, we

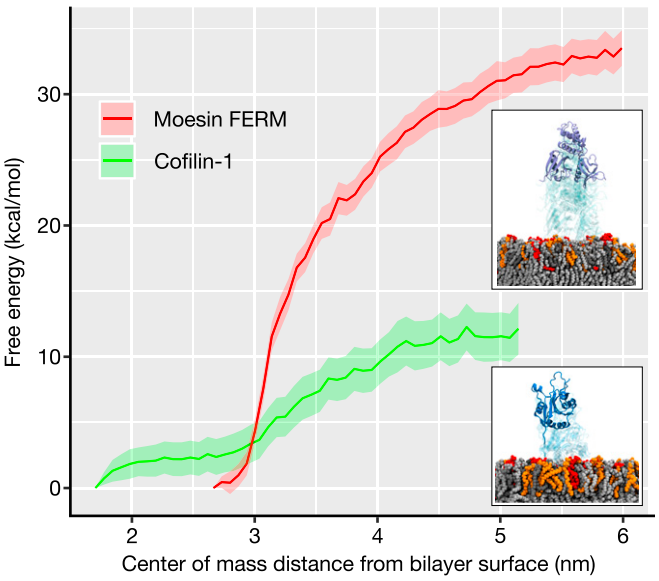

Fig. 5. Potential of mean forces for membrane associations: Cofilin-1 (green) and the moesin FERM domain (red). The final values correspond to the free energy of binding, as estimated by atomistic umbrella sampling simulations, yielding 12 ± 2 kcal/mol for cofilin and 33 ± 2 kcal/mol for the FERM domain of moesin.

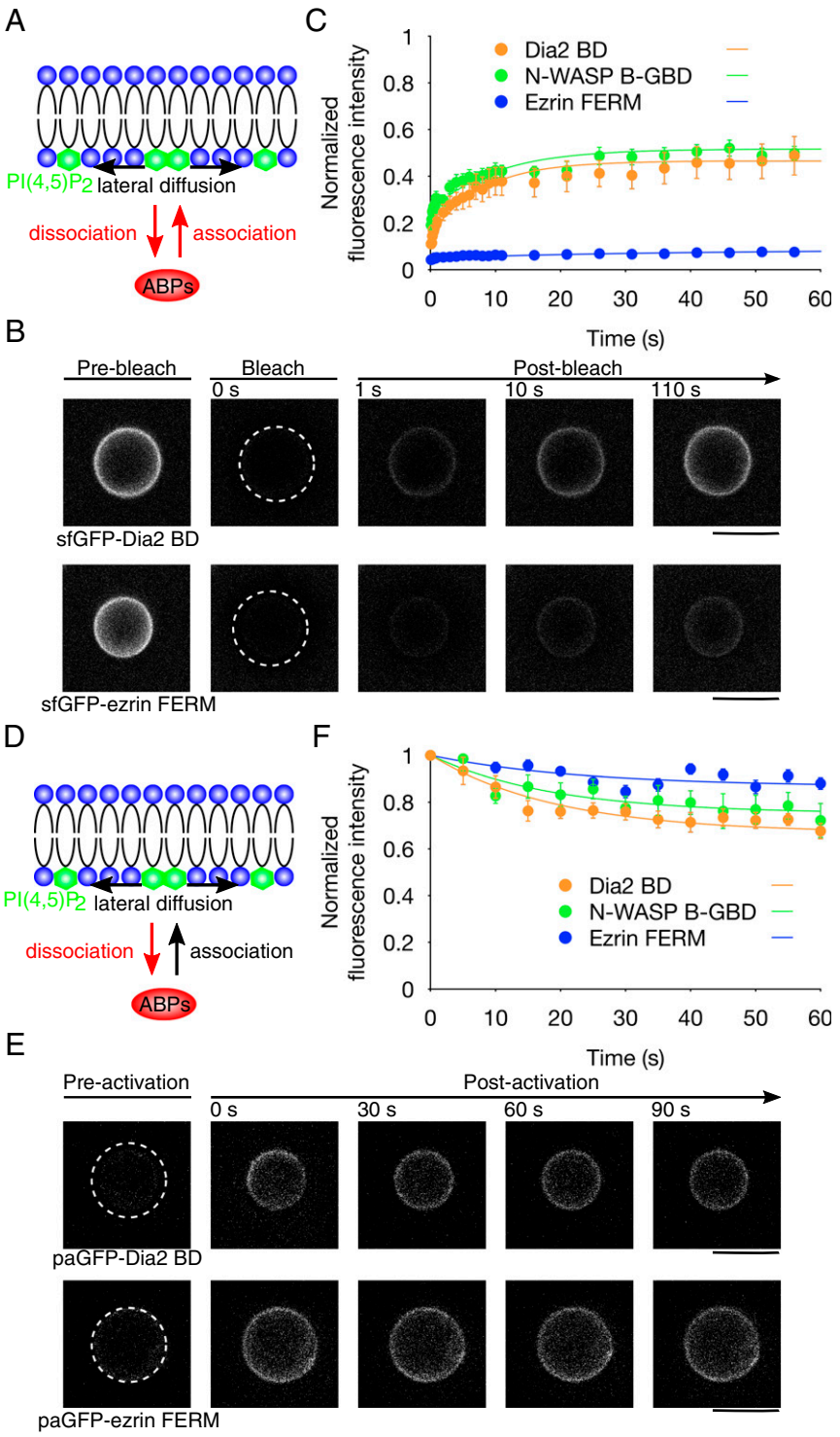

Fig. 6. Dynamics of ABPs on PI(4,5)P_2-containing membranes. (*A*) Schematic representation of the membrane association and dissociation of ABPs, as revealed by FRAP experiments. When the entire GUV is photobleached, the contribution from lateral diffusion (black) can be excluded, and the fluorescence recovery rate reflects the combination of the k_{on} and k_{off} rates (red). (*B*) Representative examples of FRAP experiments performed with sfGFP-tagged Dia2 (*Upper*) and sfGFP-tagged ezrin FERM domain-bound GUVs (*Lower*). The ABPs were applied to the outside of the GUVs, the entire GUVs (dotted line) were photobleached, and fluorescent recovery was subsequently observed. The numbers indicate the time in seconds after photobleaching. The lipid composition of the GUVs was POPC:POPE:POPS:PI(4,5)P_2:rhodamine DHPE (50:19.5:20:10:0.5, mol/mol). (Scale bar, 10 μm.) (*C*) Fluorescence recoveries of sfGFP-tagged ABPs on GUVs. The fluorescence intensities were normalized to prebleaching values, and the data were fitted with exponential curves (n = 10; mean ± SE). (*D*) Schematic representation of the membrane dissociation of ABPs, as determined by photoactivation experiments. When the protein is photoactivated on the entire GUV, the fluorescence decay should correlate with the k_{off} rate (red), whereas the k_{on} rate and lateral diffusion (black) should not contribute to the decay. (*E*) The paGFP-tagged ABPs (representative examples of Dia2 BD and ezrin FERM domain are shown in the figure) were applied to the outside of GUVs, the entire GUVs (dotted line) were photoactivated, and fluorescence decays were measured. The lipid composition of GUVs was POPC:POPE:POPS:PI(4,5)P_2:rhodamine DHPE (50:19.5:20:10:0.5, mol/mol). (Scale bar, 10 μm.) (*F*) Fluorescence decay of the activated paGFP-tagged ABPs on GUVs were measured and normalized to the initial value obtained immediately after photoactivation. The data were fitted with exponential curves (n = 10; mean ± SE).

revealed that ezrin, N-WASP, and Dia2 display surprisingly stable membrane association, and that ezrin can limit the lateral diffusion of PI(4,5)P_2 along the lipid bilayer.

Previous studies on ABPs, including ADF/cofilins, provided controversial data concerning the roles of electrostatic interactions, specific binding pockets, and lipid acyl chains in membrane interactions (36, 40). Our experiments provide strong evidence that all ABPs tested here, including cofilin-1, interact with membranes through electrostatic interactions. DPH anisotropy assays, together with atomistic molecular dynamics simulations performed on cofilin-1 and the FERM domain of moesin, provided no evidence for presence of binding pockets or for interactions with the acyl-chain region of the lipid bilayer. Moreover, the atomistic simulations revealed that cofilin-1 and the moesin FERM domain associate simultaneously with several ($n \sim 3$–6) phosphoinositide head groups. The fact that ABPs interact simultaneously with several phosphoinositide head groups also explains why they do not generally bind isolated phosphoinositide head groups (e.g., IP_3) (7) and how they can function as sensors of phosphoinositide density (36, 38) (Fig. S3).

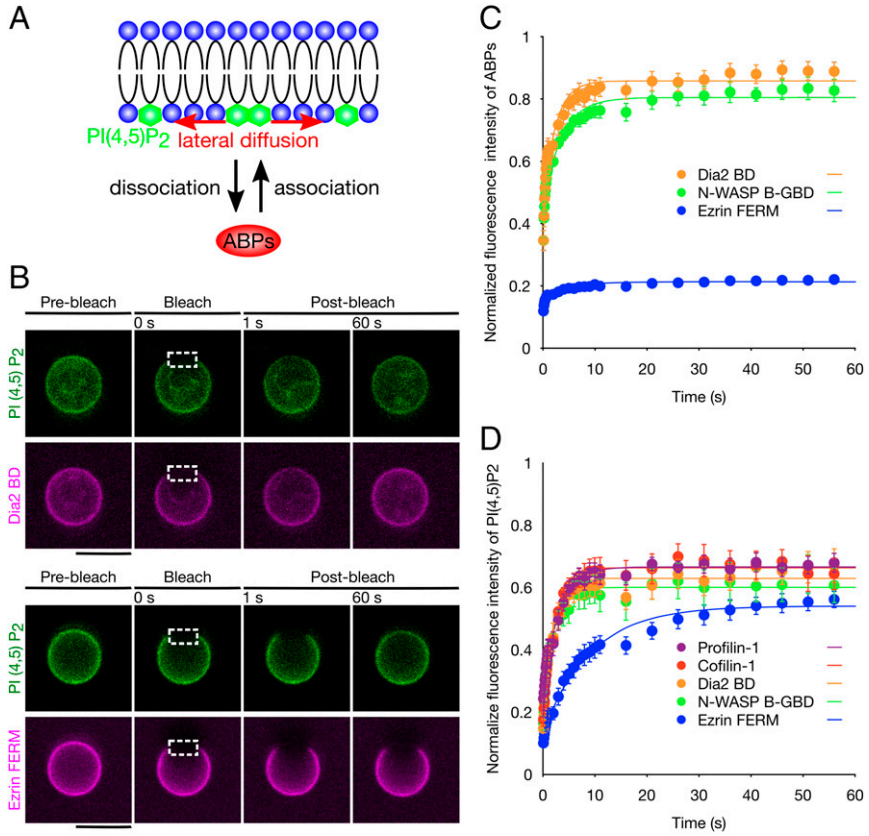

Fig. 7. Lateral diffusion of ABPs and PI(4,5)P_2 on the membrane. (*A*) Schematic representation of the lateral diffusion of ABPs and PI(4,5)P_2, as revealed by FRAP experiments. When a segment of GUV that is coated with an mCherry-tagged protein with a slow k_{off} rate from the membrane is photobleached, the fluorescence recovery rate in the photobleached area is dominated by lateral diffusion of the protein on the membrane. (*B*) Examples of fluorescence recoveries of TopFluor-labeled PI(4,5)P_2 containing GUVs incubated with mCherry-tagged lipid-binding domains of Dia2 and ezrin followed by partial photobleaching on the GUVs (dotted rectangle). The lipid composition of GUVs was POPC:POPE:POPS:PI(4,5)P_2 (58:20:20:2, mol/mol). (Scale bar, 10 μm.) (*C*) The fluorescence recovery curves of mCherry-tagged ABPs, indicating lateral diffusion, were measured and normalized. The data sets were fitted with exponential curves. Note that lateral diffusion of the FERM domain of ezrin was much slower than that of the lipid-binding domains of Dia2 and N-WASP ($n = 10$; mean ± SE). (*D*) Normalized fluorescence recoveries of TopFluor-labeled PI(4,5)P_2 on GUVs, which were incubated with 10 μM mCherry-tagged ABPs. The data sets were fitted with exponential curves. Note that lateral diffusion of TopFluor PI(4,5)P_2 at the vesicles coated with the FERM domain of ezrin was significantly slower than the vesicles incubated with profilin-1, cofilin-1, and lipid-binding domains of Dia2 and N-WASP ($n = 10$; mean ± SE).

Strikingly, although these ABPs interact with membranes through similar electrostatic mechanisms, their affinities toward phosphoinositide-rich membranes exhibit enormous differences. Interactions between these proteins and membranes are multivalent and simultaneously employ a variable number of head groups; hence, it is not possible to calculate the absolute K_d values for these interactions. However, the apparent K_d values estimated from the cosedimentation experiments carried out at 10 mol% PI(4,5)P_2 demonstrate that ezrin and moesin bind lipids with higher affinity, by an order of magnitude, compared with Dia2 and N-WASP. Furthermore, cofilin-1 and profilin-1 display more than 10-fold lower affinity for membranes compared with Dia2 and N-WASP. The low affinities of profilin-1 and cofilin-1 detected here do not seem to arise from the source of the protein or a specific isoform, because recombinant cofilin-2 as well as profilin-1 purified from bovine spleen displayed similar low-affinity membrane binding. In this context, it is important to note that when the PI(4,5)P_2 density was much higher (>20 mol%), cofilin-1 and profilin-1 displayed more pronounced, although still relatively low-affinity, binding to membranes.

Our in vitro imaging approaches uncovered the kinetics of ABP–membrane interactions. These assays revealed an extremely stable interaction of ezrin FERM domain with the membrane. In addition, Dia2 and N-WASP displayed slow dissociation from the membrane, although, based on the photoactivation assay, they dissociate more rapidly from the membrane compared with ezrin. We could not perform FRAP and photoactivation experiments for cofilin-1 and profilin-1 as a result of their very weak signals on the GUVs (Fig. 1*D*). However, the low-affinity lipid binding in vitro (Fig. 1) and experiments carried out on cells (45) (Fig. S7) are consistent with highly dynamic, transient interactions of cofilin-1 and profilin-1 with phosphoinositide-rich membranes. Furthermore, the k_{off} rate estimated from the Gibbs free energy of cofilin-1 (Fig. 5) corresponds to an off-rate on the order of 1 s^{-1}, which agrees satisfactorily with the apparent K_d value obtained from cosedimentation assays (Fig. 1), and thus provides further evidence for the rapid turnover of cofilin-1 on the membrane.

It is also interesting to note that the FERM domain of ezrin displayed very slow lateral diffusion along the membrane, and diminished the mobility of PI(4,5)P_2 by approximately fourfold. These findings may be a result of oligomerization of the FERM domain on the membrane, as previously shown for membrane-sculpting BAR superfamily domains (41, 46, 47). Oligomerization of the ezrin FERM domain on the membrane is supported by its nonhomogenous distribution on the surfaces of a fraction of GUVs (Fig. S8 *A* and *B*). It is possible that oligomerization of the FERM domain on the membrane increases its affinity by clustering PI(4,5)P_2 and by increasing the local PI(4,5)P_2 density, which may explain why the atomistic simulations provided only a few-fold higher binding free energy compared with cofilin-1, whereas the in vitro assays revealed more than two orders of magnitude higher affinity for the FERM domain with the

membrane. However, it remains to be shown whether full-length ezrin can also form oligomers on the membrane or if this property is only specific to the isolated FERM domain.

Our data provide important insights into the cellular functions and regulation of central ABPs (Fig. 8). Ezrin and moesin serve as linkers between the cortical actin cytoskeleton and the plasma membrane (48). Our data revealing very stable, high-affinity interactions of ezrin and moesin with membranes are in good agreement with their cellular function as cytoskeleton–plasma membrane cross-linkers. Furthermore, the interactions of ezrin and moesin with membranes saturate at a low PI(4,5)P_2 density (2 mol%), which is close to the "unstimulated" concentration of this phosphoinositide at the plasma membrane (49). Thus, interactions of ezrin and moesin with the cell cortex do not appear to require stimulus-responsive PI(4,5)P_2 production. In addition, Dia2 and N-WASP, which promote stimulus-responsive actin filament assembly at specific regions of the plasma membrane (50), display relatively high-affinity, stable interactions with membranes. However, in contrast to ezrin and moesin, they exhibit rapid lateral diffusion along the membrane and require a much higher PI(4,5)P_2 density for strong binding. These features agree with their cellular functions. Dia2 and N-WASP promote actin filament assembly on the plasma membrane, and stable association with membranes is therefore beneficial. On the contrary, unrestricted lateral diffusion may be important for their ability to catalyze several cycles of actin filament nucleation at the membrane. Rapid lateral diffusion is also consistent with the rapid dynamics of full-length N-WASP, as examined at the sites of extensive actin filament assembly in cells (51). Furthermore, the requirement of a relatively high PI(4,5)P_2 density (5–10 mol%) for strong binding may ensure that these proteins are activated only at specific cell regions, such as lamellipodia where the PI(4,5)P_2 concentration is high (52). Finally, our experiments provide evidence that ADF/cofilins and profilin-1 display only very transient, low-affinity interactions with membranes. At least in the case of ADF/cofilins, this is in good agreement with the cellular function, because ADF/cofilins promote severing of "aged" actin filaments that are likely positioned away from the membrane (53, 54). Thus, our data suggest that, rather than serving as a reservoir for ADF/cofilins, phosphoinositide-dense domains of the plasma membrane may serve as regions where actin filament disassembly is inhibited through transient interactions of ADF/cofilins with the membrane.

Collectively, our study uncovers the molecular principles by which central ABPs associate with phosphoinositide-rich membranes. However, it is important to note that the situation in cells is much more complex because, in addition to lipids, these proteins interact with actin and other proteins, and their activities can be controlled through signal-responsive protein–protein interactions and posttranslational modifications. Moreover, because these proteins may affect each other's mobility on the membrane and they compete with each other for phosphoinositide binding (Fig. S8 *E* and *F*), the membrane interactions of these and other phosphoinositide-associating proteins are interlinked in cells. Thus, in the future, it will be important to develop approaches that enable determining the membrane-interaction kinetics of ABPs in the complex environment of cells.

Materials and Methods

Subcloning. Sequences encoding mouse profilin-1, mouse cofilin-1, mouse cofilin-2, mouse Dia2 BD (20), rat N-WASP B-GBD (38), human ezrin FERM domain, and human moesin FERM domain were subcloned into the pGEX6P-1 vector (GE Life Sciences) with or without N-terminal sfGFP, mCherry, or paGFP tags. sfGFP is the monomeric form of GFP, and efficient folding produces a brighter signal than does EGFP (55). For mammalian expression, mouse cofilin-1, rat N-WASP B-GBD, and human ezrin FERM domain were subcloned into the sfGFP-C1 vector. sfGFP-C1 was a gift from Michael Davidson, Florida State University, Tallahassee, FL (plasmid no. 54579; Addgene). For domain-swap experiments, the sequences encoding Dia2 FH1-FH2-DAD or moesin FERM domain-fused Dia2 FH1-FH2-DAD were subcloned into the pcDNA3.1(–) vector (Thermo Fisher Scientific) containing a C-terminal HA-tag sequence.

Protein Purification. Plasmids were transformed into BL21(DE3)-competent cells, and protein expression was induced with isopropyl-D-1-thiogalactopyranoside. After collecting the cells, the pellets were sonicated in a buffer containing 20 mM Tris·HCl (pH 7.5), 150 mM NaCl,1 mM PMSF, and 1 mM DTT, followed by affinity purification with Glutathione Sepharose 4B (GE Life Sciences). The GST-tag was removed with PreScission protease (GE Life Sciences). Cofilin-1, cofilin-2, and profilin-1 were further purified with a Superdex 75 gel filtration column (GE Life Sciences) with an ÄKTA FPLC Protein Purification System (GE Life Sciences). Other proteins were purified with HiTrap SP HP or HiTrap Q HP columns (GE Life Sciences) with the ÄKTA FPLC system, depending on their theoretical pI. Proteins were concentrated using Amicon Ultra Centrifugal Filters (EMD Millipore) by replacing the buffer with 20 mM Tris·HCl (pH 7.5), 150 mM NaCl, and 1 mM DTT. Purified proteins were frozen with liquid nitrogen and stored at –80 °C.

Lipids. We purchased 1-palmitoyl-2-oleoyl-sn-glycero-3-phosphocholine (POPC), 1-palmitoyl-2-oleoyl-sn-glycero-3-phosphoethanolamine (POPE), 1-palmitoyl-2-oleoyl-sn-glycero-3-phospho-L-serine (sodium salt; POPS), TopFluor PI(4,5)P2, L-α-phosphatidylinositol-4,5-bisphosphate [brain, porcine; ammonium salt; brain PI(4,5)P2], and other phosphoinositides from Avanti Polar Lipids. Lissamine rhodamine B 1,2-dihexadecanoyl-sn-glycero-3-phosphoethanolamine, triethylammonium salt (rhodamine DHPE), and 1-(4-trimethylammoniumphenyl)-6-phenyl-1,3,5-hexatriene p-toluenesulfonate were purchased from Thermo-Fisher Scientific. The concentration of the PI(4,5)P_2 stock solution was determined based on a phosphate assay (56).

Liposome Cosedimentation/Coflotation Assays. Multilamellar vesicles (MLVs) were prepared as previously described (41). Briefly, a 1-mM lipid solution of POPC:POPE:POPS:PI(4,5)P_2:rhodamine DHPE (50:19.5:20:10:0.5, mol/mol) was prepared, dried under a stream of nitrogen gas, and hydrated in 20 mM Hepes (pH 7.5) with 100 mM NaCl. Other lipid compositions are indicated in the relevant figure legends. The addition of phosphoinositides was counteracted by the reduction of an equal molar concentration of POPC. Liposome cosedimentation and coflotation assays were performed as previously described (41, 57) with concentrations of 1 mM lipids and 1 μM ABPs unless otherwise indicated in the figure legends. ABPs were precleared with spinning at 100,000 rpm for 10 min at 4 °C with an Optima MAX Ultracentrifuge

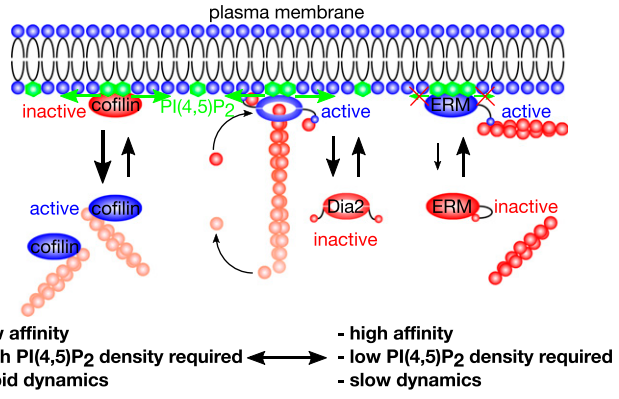

Fig. 8. A working model for interactions of ABPs with PI(4,5)P_2-containing membranes. Profilin and cofilin display only transient, low-affinity interactions with the membrane. Thus, these proteins are not sequestered at the plasma membrane, but mainly function at a distance from the membrane to carry out their roles in actin filament disassembly and monomer recycling. Dia2 and N-WASP, on the contrary, display relatively stable, high-affinity interactions with the membrane. Their interactions with PI(4,5)P_2 and other ligands release autoinhibitory structures and activate these proteins to promote actin filament assembly at the plasma membrane. Dia2 and N-WASP can undergo rapid lateral diffusion along the membrane, which may facilitate their ability to drive multiple rounds of filament assembly at the plasma membrane. Ezrin, radixin, and moesin (ERM) display very strong and stable interactions with the membrane. Additionally, the lateral diffusion of these proteins on the membrane is slow. Importantly, whereas cofilin, profilin, Dia2, and N-WASP require a stimulus-responsive high PI(4,5)P_2 density for efficient membrane interactions, ezrin and moesin bind the plasma membrane strongly even when the PI(4,5)P_2 density is low (~2 mol%), corresponding to the density of this lipid under unstimulated conditions.

equipped with a TLA-100 rotor (Beckman Coulter) to remove aggregates. The data obtained from the liposome cosedimentation assays were fitted with the nonlinear least-squares method with $y = V_{max} \times [x]/(K_d + [x])$ to estimate the equilibrium dissociation constant K_d or the Hill equation $y = V_{max} \times [x]^{nH}/(K_d{}^{nH} + [x]^{nH})$ to estimate nH. Because the proteins are accessible to only the outer leaflet of the membrane, the lipid concentration was reduced by half to calculate the K_d.

DPH Anisotropy Assay. DPH anisotropy was measured with an LS-55 fluorescence spectrometer (PerkinElmer) as previously described (41) with a 40-μM lipid solution with the composition of POPC:POPE:POPS:PI(4,5)P2:DPH (50:20:20:10:0.002, mol/mol). To obtain LUVs, the MLVs were extruded through a polycarbonate filter (100-nm pore size) by using a miniextruder (Avanti Polar Lipids). The buffer was composed of 20 mM Hepes and 100 mM NaCl (pH 7.5).

Atomistic Molecular Dynamics Simulations. All molecular dynamics simulations were performed by using the CHARMM36 force field for proteins and lipids (58, 59) and the TIP3P-CHARMM model for water (60). Protein structures for cofilin-1 and the moesin FERM domain were taken from the Protein Data Bank (ID codes 1Q8G and 1E5W). We used several $10 \times 10\text{-nm}^2$ square lipid bilayers (61), in which the upper leaflet interacting with the protein had a lipid composition of POPC:POPE:POPS:PI(4,5)P_2 (50:20:20:10, mol/mol) matching the lipid content of membranes studied in experiments (except for rhodamine, which was not included in the simulation models). The lower leaflet was composed purely of POPC to avoid an excess negative charge in the system. The unbiased simulations were conducted with 100 mM NaCl to be consistent with conditions in experiments. The free energy calculations were carried out at a slightly lower NaCl concentration (50 mM) to avoid excess charge screening and to speed up convergence. The systems were always well solvated as a result of the large dimension in the direction perpendicular to the membrane plane, as required for the potential of mean force (i.e., free energy) calculations (114 and 133 water molecules per lipid for cofilin-1 and the FERM domain of moesin, respectively).

The simulations were performed in the NPT ensemble by using Gromacs 5.0.4 (62). The reference temperature for all systems was kept constant at 303 K by using the Nose–Hoover thermostat (63, 64) with a time constant of 1 ps. The temperature of the protein, lipids, and solvent molecules were controlled independently. The pressure coupling was achieved with a Parrinello–Rahman semi-isotropic barostat (65) with a coupling constant of 1 ps and a reference pressure of 1 bar. The equations of motion were integrated with a time step of 2 fs. The LINCS algorithm (66) constrained all bonds involving hydrogens. A cutoff radius of 1.2 nm was used to switch off van der Waals interactions, whereas the smooth particle mesh Ewald technique (67) was employed to calculate long-range Coulomb interactions.

The unbiased atomistic simulation program comprised eight simulations. First, three independent 200-ns simulations were carried out for cofilin-1 and the moesin FERM domain, starting from a conformation where the residues known to be important in lipid interactions were facing the membrane and the distance between this lipid-binding patch and the membrane was ∼0.5 nm. For further sampling, one 500-ns simulation for both proteins was conducted in a similar manner but with a distance of ∼1.5 nm from the membrane. At the setup of every new replicate, the lipids underneath the protein were randomly shuffled, providing a different initial lipid distribution each time.

Protein–Lipid Contacts. A contact between a protein residue and a lipid was considered to be established (*i*) for hydrophobic residues when any carbon atom of the residue was within 0.4 nm from any carbon atom of the lipid and (*ii*) for polar/charged residues when any nitrogen or oxygen atom of the residue was within 0.35 nm from any nitrogen or oxygen atom of the lipid to account for a possible hydrogen bond. A hydrogen bond was considered to be established when the distance between donor and acceptor was 0.32 nm or less and the deviation of the donor hydrogen acceptor from linearity was 20° or less. Nitrogens and oxygens were considered as potential donors if they were bound to a hydrogen atom or as acceptors if not. For each simulation, results were computed for the equilibrated part of the trajectory and then averaged. For each model, the error bars are the SE based on averages given by the three independent simulations.

Free Energy Calculations. The calculations for the potential of mean force followed the same protocol as in ref. 68. First, an unbiased 200-ns simulation was performed for each protein to allow them to adsorb to the membrane surface and to equilibrate the binding site on the bilayer surface. When the protein had equilibrated in an appropriate orientation at the membrane surface, corresponding to its free energy minimum bound to the membrane surface, the protein was slowly pulled away from the bilayer to the water phase. By using the trajectory generated during the pulling process, the initial configurations were generated for the umbrella sampling simulations. The umbrella sampling calculation was based on a total of 62 and 57 windows for cofilin-1 and the FERM domain of moesin, respectively, with the windows separated from each other by 0.04–0.05 nm (the initial separation was 0.5 nm with later additions of extra intermediate windows to improve the overlap of the umbrella histograms). Each window was simulated for 50 ns, of which the leading 10 ns was used for equilibration and the rest (40 ns) was used for analysis. For the analysis, we used the weighted histogram analysis method (69) as implemented in Gromacs 5.0.4. The errors were estimated by bootstrap analysis.

FRAP and Photoactivation Experiments. GUVs at a physiological salt concentration were prepared as previously described (70). The lipid composition was POPC:POPE:POPS:PI(4,5)P_2:rhodamine DHPE (50:19.5:20:10:0.5, mol/mol) or POPC:POPE:POPS:PI(4,5)P_2:TopFluor PI(4,5)P_2 (58:20:20:10:1:1, mol/mol). The buffer composition outside of the GUVs was 5 mM Hepes (pH 7.5), 100 mM NaCl, and 200 mM glucose, whereas that inside the GUVs was 5 mM Hepes (pH 7.5), 100 mM NaCl, and 200 mM sucrose. The osmolarities of the buffers (inside and outside of the GUVs) were adjusted by using an osmometer. The coverslips were coated with β-casein (Sigma-Aldrich) to avoid nonspecific protein binding.

The FRAP assay was performed with a TCS SP5 confocal microscope (Leica) in a region of interest (ROI) with 488-nm or 561-nm lasers. To measure the lateral diffusion of proteins and PI(4,5)P_2, we photobleached 5.0×2.5-μm ROIs. The time course of changes in the fluorescence intensity in the ROI after photobleaching was followed by using excitation light at the minimum intensity possible to minimize subsequent photobleaching. After background subtraction, the data were fitted with the nonlinear least-squares method using the equation $y(t) = A(1 - \exp(-t/\tau)) + B$, where t is the time after bleaching. Because the lateral diffusion of the lipid molecules is constrained to the 2D plane of the membrane, the circular area on the top of the GUVs was bleached, and the diffusion coefficient D was calculated by using the relationship $D = 0.88 \times \omega^2/(4t_{1/2})$, where ω is the radius of the area bleached and $t_{1/2}$ ($=\tau \times \ln 2$) is the half-time of the recovery.

For the photoactivation experiments, GUVs were prepared according to the same procedure as described earlier with a lipid composition of POPC:POPE:POPS:PI(4,5)P_2:rhodamine DHPE (50:19.5:20:10:0.5, mol/mol). Photoactivation was performed by using a TCS SP5 confocal microscope (Leica) with a 405-nm laser, and the subsequent activated fluorescence was observed with a 488-nm laser.

Cell Culture and FRAP. B16-F1 cells were cultured in DMEM supplemented with 10% FBS (Invitrogen), L-glutamine (Sigma-Aldrich), and penicillin/streptomycin (Sigma-Aldrich). Transfections were performed with FuGENE HD (Promega) using Opti-MEM (Invitrogen) in the absence of antibiotics according to the manufacturer's protocol.

Anti-HA antibody produced in rabbit (Sigma-Aldrich), Alexa 488 goat anti-rabbit IgG (heavy and light chains) highly cross-adsorbed secondary antibody (Thermo Fisher Scientific), and Alexa Fluor 568 phalloidin (Thermo Fisher Scientific) were used for general immunofluorescence protocol. Images were acquired by using an LSM 700 laser scanning confocal microscope (Carl Zeiss) with objective LCI Plan-Neofluar 63×/1.3 Imm Corr DIC.

For the FRAP experiments performed with an SP5 confocal microscope (Leica) with Leica objective (HC PL APO 63×/1.20 W CORR CS2), the cells were cultured on glass-bottom dishes (Greiner Bio-One) coated with laminin (Sigma-Aldrich). The FRAP experiments were performed with a 488-nm Ar laser at 37 °C and 5% CO_2. After photobleaching, the laser power was decreased to as low as possible to minimize the extent of photobleaching during the observation period. The time course of changes in the fluorescence intensity in the ROI after photobleaching was quantified by using ImageJ software (National Institutes of Health).

ACKNOWLEDGMENTS. We thank Patricia Bassereau, Feng-Ching Tsai (Institut Curie, France), Elina Ikonen, and Maarit Neuvonen (Faculty of Medicine, University of Helsinki) for their helpful discussions and technical advice. The authors also thank the Light Microscopy Unit (Institute of Biotechnology, University of Helsinki), Lotta Gustavsson, Aleksi Ainonen, Markus Korpela, and Anna Liisa Nyfors for technical assistance. The Dia2 and N-WASP cDNAs were kind gifts from Tatyana Svitkina (University of Pennsylvania) and Jack Taunton (University of California, San Francisco), respectively. The cDNAs for ezrin and moesin were provided by the Genome Biology Unit (Biocenter Finland, University of Helsinki). This work was supported by the Academy of Finland (Center of Excellence program; Y.S., M.K., I.V., and P.L.), the Japan Society for the Promotion of Science (Y.S.), and European Research Council Advanced Grant CROWDED-PRO-LIPIDS (to I.V.). We acknowledge the Finnish CSC-IT Centre for Science (Espoo, Finland) for computer resources.

1. Weinberg J, Drubin DG (2012) Clathrin-mediated endocytosis in budding yeast. *Trends Cell Biol* 22:1–13.
2. Blanchoin L, Boujemaa-Paterski R, Sykes C, Plastino J (2014) Actin dynamics, architecture, and mechanics in cell motility. *Physiol Rev* 94:235–263.
3. Chhabra ES, Higgs HN (2007) The many faces of actin: Matching assembly factors with cellular structures. *Nat Cell Biol* 9:1110–1121.
4. Pollard TD, Cooper JA (2009) Actin, a central player in cell shape and movement. *Science* 326:1208–1212.
5. Bugyi B, Carlier M-F (2010) Control of actin filament treadmilling in cell motility. *Annu Rev Biophys* 39:449–470.
6. Saarikangas J, Zhao H, Lappalainen P (2010) Regulation of the actin cytoskeleton-plasma membrane interplay by phosphoinositides. *Physiol Rev* 90:259–289.
7. Yonezawa N, Nishida E, Iida K, Yahara I, Sakai H (1990) Inhibition of the interactions of cofilin, destrin, and deoxyribonuclease I with actin by phosphoinositides. *J Biol Chem* 265:8382–8386.
8. Janmey PA, Stossel TP (1987) Modulation of gelsolin function by phosphatidylinositol 4,5-bisphosphate. *Nature* 325:362–364.
9. Palmgren S, Ojala PJ, Wear MA, Cooper JA, Lappalainen P (2001) Interactions with PIP2, ADP-actin monomers, and capping protein regulate the activity and localization of yeast twinfilin. *J Cell Biol* 155:251–260.
10. Schafer DA, Jennings PB, Cooper JA (1996) Dynamics of capping protein and actin assembly in vitro: Uncapping barbed ends by polyphosphoinositides. *J Cell Biol* 135:169–179.
11. Prehoda KE, Scott JA, Mullins RD, Lim WA (2000) Integration of multiple signals through cooperative regulation of the N-WASP-Arp2/3 complex. *Science* 290:801–806.
12. Rohatgi R, Ho HY, Kirschner MW (2000) Mechanism of N-WASP activation by CDC42 and phosphatidylinositol 4, 5-bisphosphate. *J Cell Biol* 150:1299–1310.
13. Barret C, Roy C, Montcourrier P, Mangeat P, Niggli V (2000) Mutagenesis of the phosphatidylinositol 4,5-bisphosphate (PIP(2)) binding site in the NH(2)-terminal domain of ezrin correlates with its altered cellular distribution. *J Cell Biol* 151: 1067–1080.
14. Martel V, et al. (2001) Conformation, localization, and integrin binding of talin depend on its interaction with phosphoinositides. *J Biol Chem* 276:21217–21227.
15. Higgs HN, Pollard TD (2000) Activation by Cdc42 and PIP(2) of Wiskott-Aldrich syndrome protein (WASp) stimulates actin nucleation by Arp2/3 complex. *J Cell Biol* 150: 1311–1320.
16. Yamamoto M, et al. (2001) Phosphatidylinositol 4,5-bisphosphate induces actin stress-fiber formation and inhibits membrane ruffling in CV1 cells. *J Cell Biol* 152:867–876.
17. Raucher D, et al. (2000) Phosphatidylinositol 4,5-bisphosphate functions as a second messenger that regulates cytoskeleton-plasma membrane adhesion. *Cell* 100: 221–228.
18. Rozelle AL, et al. (2000) Phosphatidylinositol 4,5-bisphosphate induces actin-based movement of raft-enriched vesicles through WASP-Arp2/3. *Curr Biol* 10:311–320.
19. Cunningham CC, et al. (2001) Cell permeant polyphosphoinositide-binding peptides that block cell motility and actin assembly. *J Biol Chem* 276:43390–43399.
20. Gorelik R, Yang C, Kameswaran V, Dominguez R, Svitkina T (2011) Mechanisms of plasma membrane targeting of formin mDia2 through its amino terminal domains. *Mol Biol Cell* 22:189–201.
21. van Rheenen J, et al. (2007) EGF-induced PIP2 hydrolysis releases and activates cofilin locally in carcinoma cells. *J Cell Biol* 179:1247–1259.
22. Chinthalapudi K, et al. (2014) Lipid binding promotes oligomerization and focal adhesion activity of vinculin. *J Cell Biol* 207:643–656.
23. Rivera GM, Vasilescu D, Papayannopoulos V, Lim WA, Mayer BJ (2009) A reciprocal interdependence between Nck and PI(4,5)P(2) promotes localized N-WASp-mediated actin polymerization in living cells. *Mol Cell* 36:525–535.
24. Wollman R, Meyer T (2012) Coordinated oscillations in cortical actin and Ca2+ correlate with cycles of vesicle secretion. *Nat Cell Biol* 14:1261–1269.
25. Rousso T, Shewan AM, Mostov KE, Schejter ED, Shilo B-Z (2013) Apical targeting of the formin Diaphanous in Drosophila tubular epithelia. *Elife* 2:e00666.
26. Kim K, et al. (2007) Structure/function analysis of the interaction of phosphatidylinositol 4,5-bisphosphate with actin-capping protein: Implications for how capping protein binds the actin filament. *J Biol Chem* 282:5871–5879.
27. Pleskot R, Pejchar P, Žárský V, Staiger CJ, Potocký M (2012) Structural insights into the inhibition of actin-capping protein by interactions with phosphatidic acid and phosphatidylinositol (4,5)-bisphosphate. *PLoS Comput Biol* 8:e1002765.
28. Tania N, Prosk E, Condeelis J, Edelstein-Keshet L (2011) A temporal model of cofilin regulation and the early peak of actin barbed ends in invasive tumor cells. *Biophys J* 100:1883–1892.
29. Sengelaub CA, Navrazhina K, Ross JB, Halberg N, Tavazoie SF (2016) PTPRN2 and PLCβ1 promote metastatic breast cancer cell migration through PI(4,5)P2-dependent actin remodeling. *EMBO J* 35:62–76.
30. Ramalingam N, et al. (2010) Phospholipids regulate localization and activity of mDia1 formin. *Eur J Cell Biol* 89:723–732.
31. Dames SA, et al. (2011) Structure, dynamics, lipid binding, and physiological relevance of the putative GTPase-binding domain of Dictyostelium formin C. *J Biol Chem* 286: 36907–36920.
32. van Gisbergen PAC, Li M, Wu S-Z, Bezanilla M (2012) Class II formin targeting to the cell cortex by binding PI(3,5)P(2) is essential for polarized growth. *J Cell Biol* 198: 235–250.
33. Ramalingam N, et al. (2015) A resilient formin-derived cortical actin meshwork in the rear drives actomyosin-based motility in 2D confinement. *Nat Commun* 6:8496.
34. Lambrechts A, Jonckheere V, Dewitte D, Vandekerckhove J, Ampe C (2002) Mutational analysis of human profilin I reveals a second PI(4,5)-P2 binding site neighbouring the poly(L-proline) binding site. *BMC Biochem* 3:12.
35. Skare P, Karlsson R (2002) Evidence for two interaction regions for phosphatidylinositol(4,5)-bisphosphate on mammalian profilin I. *FEBS Lett* 522: 119–124.
36. Zhao H, Hakala M, Lappalainen P (2010) ADF/cofilin binds phosphoinositides in a multivalent manner to act as a PIP(2)-density sensor. *Biophys J* 98:2327–2336.
37. Goldschmidt-Clermont PJ, Machesky LM, Baldassare JJ, Pollard TD (1990) The actin-binding protein profilin binds to PIP2 and inhibits its hydrolysis by phospholipase C. *Science* 247:1575–1578.
38. Papayannopoulos V, et al. (2005) A polybasic motif allows N-WASP to act as a sensor of PIP(2) density. *Mol Cell* 17:181–191.
39. Hamada K, Shimizu T, Matsui T, Tsukita S, Hakoshima T (2000) Structural basis of the membrane-targeting and unmasking mechanisms of the radixin FERM domain. *EMBO J* 19:4449–4462.
40. Gorbatyuk VY, et al. (2006) Mapping the phosphoinositide-binding site on chick cofilin explains how PIP2 regulates the cofilin-actin interaction. *Mol Cell* 24:511–522.
41. Zhao H, et al. (2013) Membrane-sculpting BAR domains generate stable lipid microdomains. *Cell Rep* 4:1213–1223.
42. Saarikangas J, et al. (2009) Molecular mechanisms of membrane deformation by I-BAR domain proteins. *Curr Biol* 19:95–107.
43. Pope BJ, Zierler-Gould KM, Kühne R, Weeds AG, Ball LJ (2004) Solution structure of human cofilin: Actin binding, pH sensitivity, and relationship to actin-depolymerizing factor. *J Biol Chem* 279:4840–4848.
44. Edwards SD, Keep NH (2001) The 2.7 A crystal structure of the activated FERM domain of moesin: An analysis of structural changes on activation. *Biochemistry* 40: 7061–7068.
45. Lai FPL, et al. (2008) Arp2/3 complex interactions and actin network turnover in lamellipodia. *EMBO J* 27:982–992.
46. Frost A, et al. (2008) Structural basis of membrane invagination by F-BAR domains. *Cell* 132:807–817.
47. Mim C, et al. (2012) Structural basis of membrane bending by the N-BAR protein endophilin. *Cell* 149:137–145.
48. Neisch AL, Fehon RG (2011) Ezrin, radixin and moesin: Key regulators of membrane-cortex interactions and signaling. *Curr Opin Cell Biol* 23:377–382.
49. McLaughlin S, Wang J, Gambhir A, Murray D (2002) PIP(2) and proteins: Interactions, organization, and information flow. *Annu Rev Biophys Biomol Struct* 31:151–175.
50. Campellone KG, Welch MD (2010) A nucleator arms race: Cellular control of actin assembly. *Nat Rev Mol Cell Biol* 11:237–251.
51. Weisswange I, Newsome TP, Schleich S, Way M (2009) The rate of N-WASP exchange limits the extent of ARP2/3-complex-dependent actin-based motility. *Nature* 458: 87–91.
52. Golub T, Caroni P (2005) PI(4,5)P2-dependent microdomain assemblies capture microtubules to promote and control leading edge motility. *J Cell Biol* 169:151–165.
53. Okreglak V, Drubin DG (2007) Cofilin recruitment and function during actin-mediated endocytosis dictated by actin nucleotide state. *J Cell Biol* 178:1251–1264.
54. Andrianantoandro E, Pollard TD (2006) Mechanism of actin filament turnover by severing and nucleation at different concentrations of ADF/cofilin. *Mol Cell* 24:13–23.
55. Pédelacq J-D, Cabantous S, Tran T, Terwilliger TC, Waldo GS (2006) Engineering and characterization of a superfolder green fluorescent protein. *Nat Biotechnol* 24:79–88.
56. Bartlett GR (1959) Phosphorus assay in column chromatography. *J Biol Chem* 234: 466–468.
57. Kostan J, et al. (2014) Direct interaction of actin filaments with F-BAR protein pacsin2. *EMBO Rep* 15:1154–1162.
58. Best RB, et al. (2012) Optimization of the additive CHARMM all-atom protein force field targeting improved sampling of the backbone φ, ψ and side-chain χ(1) and χ(2) dihedral angles. *J Chem Theory Comput* 8:3257–3273.
59. Klauda JB, et al. (2010) Update of the CHARMM all-atom additive force field for lipids: Validation on six lipid types. *J Phys Chem B* 114:7830–7843.
60. Jorgensen WL, Chandrasekhar J, Madura JD, Impey RW, Klein ML (1983) Comparison of simple potential functions for simulating liquid water. *J Chem Phys* 79:926–935.
61. Jo S, Kim T, Iyer VG, Im W (2008) CHARMM-GUI: A web-based graphical user interface for CHARMM. *J Comput Chem* 29:1859–1865.
62. Abraham MJ, et al. (2015) GROMACS: High performance molecular simulations through multi-level parallelism from laptops to supercomputers. *SoftwareX* 1–2: 19–25.
63. Nosé S (1984) A unified formulation of the constant temperature molecular dynamics methods. *J Chem Phys* 81:511–519.
64. Melchionna S, Ciccotti G, Holian BL (1993) Hoover NPT dynamics for systems varying in shape and size. *Mol Phys* 78:533–544.
65. Parrinello M, Rahman A (1981) Polymorphic transitions in single crystals: A new molecular dynamics method. *J Appl Phys* 52:7182–7190.
66. Hess B, Bekker H, Berendsen HJC, Fraaije JGEM (1997) LINCS: A linear constraint solver for molecular simulations. *J Comput Chem* 18:1463–1472.
67. Essmann U, et al. (1995) A smooth particle mesh Ewald method. *J Chem Phys* 103: 8577–8593.
68. Lemkul JA, Bevan DR (2010) Assessing the stability of Alzheimer's amyloid protofibrils using molecular dynamics. *J Phys Chem B* 114:1652–1660.
69. Kumar S, Rosenberg JM, Bouzida D, Swendsen RH, Kollman PA (1992) The weighted histogram analysis method for free-energy calculations on biomolecules. I. The method. *J Comput Chem* 13:1011–1021.
70. Saarikangas J, et al. (2015) MIM-induced membrane bending promotes dendritic spine initiation. *Dev Cell* 33:644–659.
71. Sheu S-Y, Yang D-Y, Selzle HL, Schlag EW (2003) Energetics of hydrogen bonds in peptides. *Proc Natl Acad Sci USA* 100:12683–12687.